

Strong Magnon-Phonon Coupling in the Kagome Antiferromagnets

A. S. Sukhanov,^{1,*} O. I. Utesov^{2,†} A. N. Korshunov³ N. D. Andriushin⁴ M. S. Pavlovskii⁵ S. E. Nikitin,⁶
A. A. Kulbakov⁴ K. Manna,⁷ C. Felser⁸ and M. C. Rahn¹

¹Experimental Physics VI, Center for Electronic Correlations and Magnetism, University of Augsburg, 86159 Augsburg, Germany

²Center for Theoretical Physics of Complex Systems, Institute for Basic Science (IBS), Daejeon 34126, Republic of Korea

³Donostia International Physics Center (DIPC), Paseo Manuel de Lardizabal, 20018 San Sebastian, Spain

⁴Institut für Festkörper- und Materialphysik, Technische Universität Dresden, D-01069 Dresden, Germany

⁵Kirensky Institute of Physics, Krasnoyarsk 660036, Russian Federation

⁶PSI Center for Neutron and Muon Sciences, Paul Scherrer Institut, CH-5232 Villigen-PSI, Switzerland

⁷Indian Institute of Technology-Delhi, New Delhi, Hauz Khas, 110 016, India

⁸Max Planck Institute for Chemical Physics of Solids, D-01187 Dresden, Germany

(Received 28 January 2025; revised 17 June 2025; accepted 25 July 2025; published 21 August 2025)

Magnon-phonon hybridization in ordered materials is a crucial phenomenon with significant implications for spintronics, magnonics, and quantum materials research. We present direct experimental evidence and theoretical insights into magnon-phonon coupling in Mn₃Ge, a kagome antiferromagnet with noncollinear spin order. Using inelastic x-ray scattering and *ab initio* modeling, we uncover strong hybridization between planar spin fluctuations and transverse optical phonons, resulting in a large hybridization gap of ~ 2 meV. This coupling is driven by interlayer Heisenberg exchange interactions and is enhanced by the material's symmetry and magnetic frustration. The simplicity of the Mn₃Ge structure enables clear identification of the hybridized modes, bridging theoretical predictions and experimental observations. Our findings establish Mn₃Ge as a model system for exploring magnon-phonon interactions and offer a pathway for designing materials with tunable magnetoelastic properties.

DOI: 10.1103/gymx-jk1g

Introduction—The study of magnons and phonons plays a fundamental role in understanding the behavior of ordered materials at a microscopic level. When excitations of the lattice and spin subsystems significantly interact, they are no longer independent quasiparticles but form hybrid modes known as the magnetoelastic modes, the magnon-phonon excitations, or simply magnon polarons. The resulting excitations can lead to novel emergent properties such as the magnon-phonon Fermi resonance [1,2], the anomalous spin Seebeck effect [3–5], topological magnon polarons [6–9], or chiral phonons [10–12]. Consequently, the phenomena that allow for the mutual coherent conversion between the lattice and magnetic degrees of freedom within a material become promising for application in spintronics [13,14], magnonics [15–17], and neuromorphic computing [18,19].

In antiferromagnets (AFMs) the magnetic structure can become complex upon geometric frustration. In particular, materials with noncollinear magnetic arrangements might display strong magnon-phonon hybridization due to the lack of a global spin quantization axis, which allows for one-magnon terms in the spin Hamiltonian and can lead to a linear coupling between magnons and phonons [20,21].

The linear magnon-phonon coupling in frustrated noncollinear AFMs thus provides a fertile ground for exploring the interaction between spin and lattice degrees of freedom at the energy scales well accessible by the momentum-resolved spectroscopic techniques [22].

Despite that magnetic subsystems of many triangular AFMs can be well described by a relatively simple Hamiltonian [20,23–29], the analysis and interpretation of the hybrid modes are frequently hindered by the complexity of the bare lattice vibrations. Indeed, the unit cell may contain many nonmagnetic ions and, hence, phonons, each having its contribution to the coupled spectrum with a different strength [20,26]. Therefore, discovering a noncollinear AFM consisting of only or predominantly magnetic ions can bridge the gap between the theoretical models [6,20,21,26,30–32] and experimental data, as its lattice and magnetic fluctuations will be carried by the same atoms.

In this Letter, we chose a frustrated kagome antiferromagnet, Mn₃Ge (SG P6₃/mmc), to demonstrate, both experimentally via inelastic x-ray scattering (IXS) and theoretically via first-principle simulations and analytical derivations (see End Matter), how the exchange coupling between the kagome layers drives unique zone-centered magnon polarons. By understanding the detailed physical mechanism of such a strong coupling between the specific

*Contact author: aleksandr.sukhanov@uni-a.de

†Contact author: utiosov@gmail.com

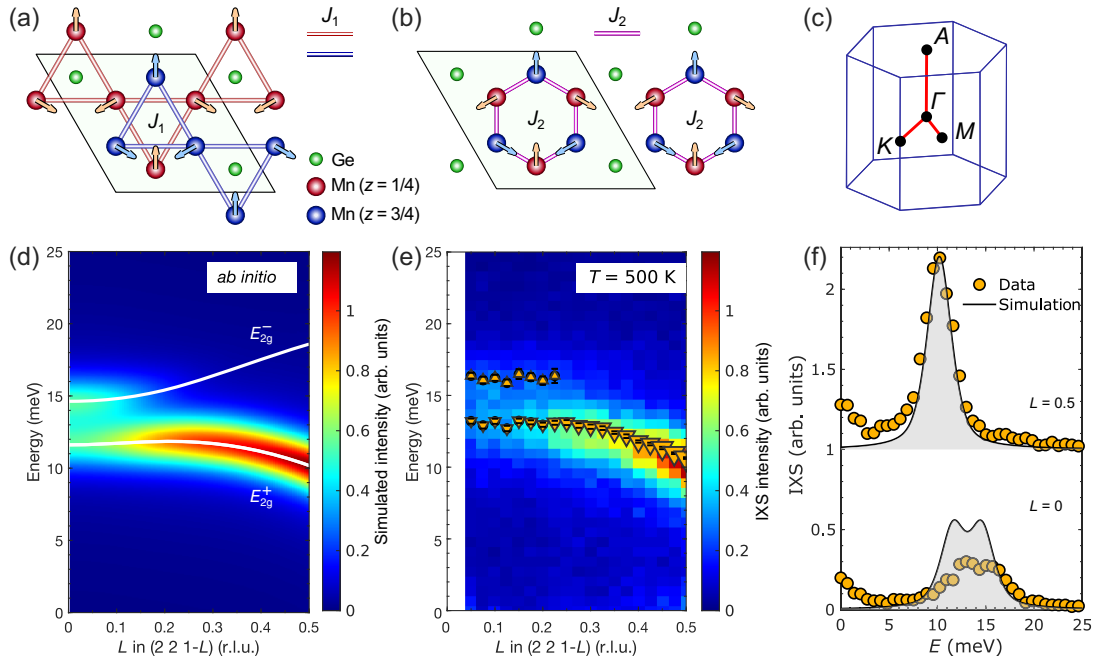


FIG. 1. (a),(b) Crystal and magnetic structures of Mn₃Ge viewed from the [001] axis. Two kagome layers spaced along *c* are colored red and blue. The bonds show exchange interaction *J*₁ (in-plane, (a) and *J*₂ [out-of-plane, (b)]. (c) First Brillouin zone of Mn₃Ge; the high-symmetry points are denoted. (d) Simulated IXS intensity of the bare phonons in the (221) zone, where only two modes are visible. (e) Experimental spectrum collected at the same zone at 500 K. The symbols are the fit results. (f) The intensity profiles (symbols) from (e) and the simulated spectra (shaded area) from (d). The data were offset by 1 arb. units for clarity.

lattice distortions and AFM spin waves, we show the simplicity and universality of such excitations and predict that the robust magnon polarons can be found in many more kagome antiferromagnets.

Structure of Mn₃Ge—Interestingly, the material received enormous attention when it was recognized as a topological Weyl semimetal [33,34] and a host to the large anomalous Hall effect [35,36]. The crystalline and magnetic structures of Mn₃Ge are shown in Figs. 1(a) and 1(b). The compound consists of the AB-stacked kagome planes. The in-plane unit-cell parameter *a* ≈ 5.4 Å is close to the out-of-plane parameter *c* ≈ 4.4 Å, so the intra and interplane exchange interactions are of the same order of magnitude. The magnetic structure for each kagome layer is the antichiral 120° order, which alternates for neighboring layers due to the AFM interaction, so the spins related by inversion align parallel [37–39]. The Néel temperature *T*_N ≈ 370 K. Mn atoms have magnetic moments of ∼2.5 μ_B . In addition, two Ge atoms are present in the unit cell (one in each kagome layer) filling the voids of the lattice. We show below that they play a minor role in the magnon-phonon coupling and can be neglected.

The model of magnetic exchange interactions in Mn₃Ge was proposed in early neutron spectroscopy studies [40]. The additional resonances at the zone center are not captured by the Heisenberg model and were interpreted by the magnetic anisotropy up to the sixth order, which is untypical for 3d elements. Subsequent neutron scattering

and theory works discussed the plausibility of the high-order single-ion anisotropies [41,42] but also pointed out that the observed spectra might be affected by the coupling between the magnetic and lattice excitations [41,43]. Note that, because neutron scattering is sensitive to both magnons and phonons, it is challenging to distinguish the uncorrelated magnetic and lattice excitations from the hybrid modes in the total scattering cross section. Therefore, alternative scattering techniques, such as IXS, can be advantageous.

The metallic nature of Mn₃Ge implies that the unpaired electrons of Mn might be itinerant. Indeed, the presence of long-range couplings was argued in Ref. [40]. However, the misinterpretations of the strongly coupled magnon-phonon spectra for the conventional magnet could have led to erroneous conclusions on its exchange parameters. For our goal—discussion of the strong magnon-phonon coupling along the high-symmetry direction—it is sufficient to account for several crucial couplings, whereas the inclusion of next-neighbor interactions is excessive [44].

Experimental spectra at high temperatures—We used the phonon eigenvectors obtained in our *ab initio* calculations (see Supplemental Material [44]) to simulate the intensity of IXS at any arbitrary momentum transfer **Q**. The simulated IXS intensities are directly proportional to the phonon spectral weight in a Brillouin zone (BZ) with particular (*HKL*) indexes. By comparing the relative intensities among various phonon branches throughout a

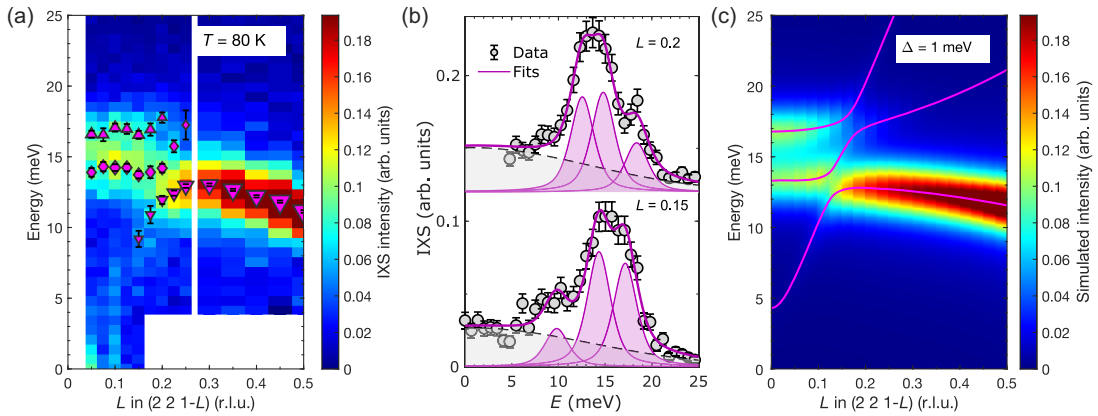


FIG. 2. (a) Experimental spectrum at $T = 80$ K. The symbols are the fit results [44]. We note that the strike of intensity at 0.1 r.l.u. is an experimental artifact [44]. (b) Intensity profiles (symbols) from (a) and the fitted peaks (shaded areas), the fitted background (dashed lines), and the overall fitting curves (black solid lines). The data were offset by 0.12 arb. units for clarity. (c) Simulated IXS intensity of the coupled magnon-phonon modes for the coupling strength $\Delta = 1$ meV. The calculated dispersion curves of the hybridized modes are plotted as solid lines over the color map of intensity.

large volume of reciprocal space (see Supplemental Material [44]), we can locate the zones at which the in-plane-polarized E_{2g} optical modes have the highest contrast. In other words, their spectral weight is much larger than that of all other branches.

It follows from our analysis that the zone center at $\mathbf{Q} = (2\bar{2}\bar{1})$ r.l.u. is the ideal reciprocal-space point for observation of the E_{2g}^- and E_{2g}^+ vibrations, as they have approximately equal intensities at the Γ point, whereas the intensities of the other modes are practically negligible (at least an order of magnitude weaker). Below it will be shown that namely these two optical modes are responsible for the formation of magnon polarons. The simulated spectra shown in Fig. 1(d) for the momenta from $(2\bar{2}\bar{1})$ to $(2\bar{2}\frac{1}{2})$ r.l.u., which correspond to the $\Gamma - A$ path of the BZ, predict a very distinct dispersion of the lower E_{2g}^+ mode. It disperses slightly upward near the zone center and then turns down as it approaches the zone boundary, where it gains higher intensity. Oppositely, the upper E_{2g}^- mode, being clearly distinct in the vicinity of the zone center, rapidly loses its spectral weight as it disperses upward.

Figure 1(e) is an experimental IXS spectrum of Mn_3Ge collected for the same momenta of $(2\bar{2}\bar{1} - L)$ r.l.u. as in theoretical Fig. 1(d). The spectrum covers the energy transfer of 0–25 meV and was measured at $T = 500$ K, which is much higher than T_N . Therefore, at such a high temperature, one expects to observe the bare phonon dispersion free from coupling with the magnons. In full agreement with such expectations, Fig. 1(e) features the two optical branches whose dispersion and spectral weight are well reproduced by our first-principle calculations. The positions of the E_{2g}^- and E_{2g}^+ IXS peaks at each momentum can be extracted by the Lorentzian fits (see Supplemental Material [44] for the details). The results of the fits are plotted over the color-coded intensity map in Fig. 1(e) for a

better comparison with the theory. The experimental energies are slightly higher than the *ab initio* predicted ones, namely, the lower branch E_{2g}^+ is located at $E \approx 13$ meV at the Γ point ($E_{\text{calc}} \approx 12$ meV), whereas the energy of the upper branch is ≈ 2 meV higher than the calculated value. Remarkably, at the zone boundary (the A point), the experimental energy of the E_{2g}^+ branch matches the theoretical one within the error bars of the fit. To demonstrate the agreement between the experimental data at $T = 500$ K and the *ab initio* results in more detail, we present the individual IXS intensity profiles as a function of energy at $L = 0$ and $L = 0.5$ r.l.u. (the BZ center and the BZ boundary, respectively) in Fig. 1(f). For a direct comparison, the simulated intensity was convoluted with the experimental resolution. It should be noted that the intensity of the experimental peaks at $L = 0$ is somewhat below the theory prediction, which may be related to additional anisotropic sample absorption and/or slight rotation of the factual displacement vectors of the mode with respect to the theoretically predicted ones.

Low-temperature magnon polarons—Having verified that the experimental data at $T > T_N$ is well reproduced by the bare phonon modes obtained from our *ab initio* calculations, we can study Mn_3Ge at a low temperature $T \ll T_N$. In particular, we observe how its spectra alter due to the magnetoelastic coupling.

Indeed, the spectrum collected at 80 K for the same reciprocal space direction [Fig. 2(a)] drastically differs from the data at the high temperature. At the zone center, we observe the same two excitations of equal intensities, yet their energies shifted up by ~ 1 meV. The two modes are nearly flat up to momenta of $L = 0.15$ r.l.u.; afterward they rapidly acquire a steep upward dispersion. The observed phonon spectral weight of the middle mode is lost shortly after the momentum at which the bare magnons

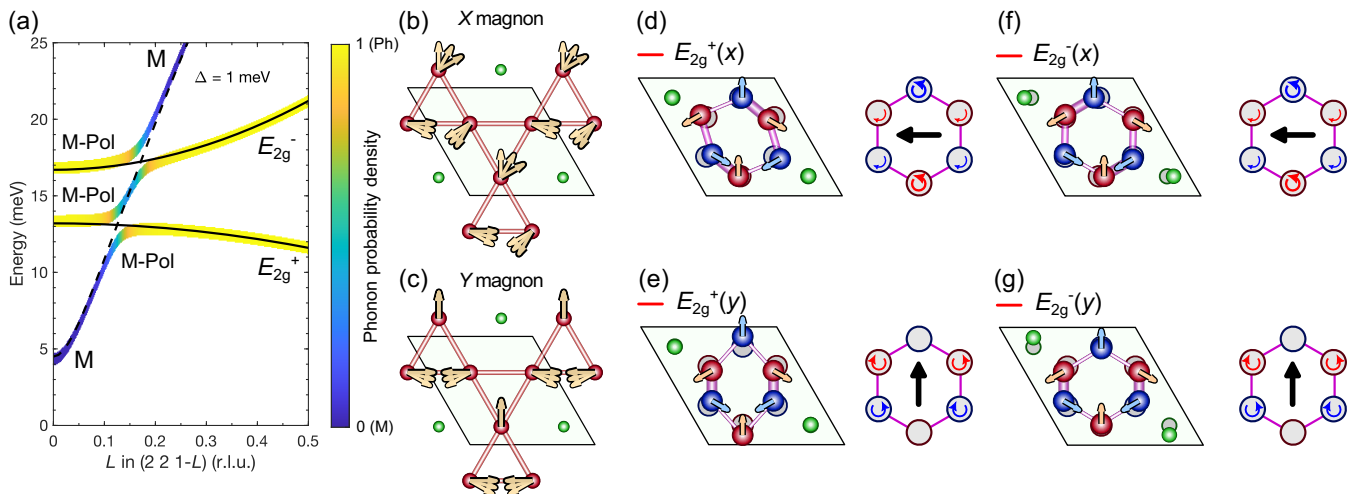


FIG. 3. (a) Magnon-phonon dispersion colored by relative contributions of the magnons (blue) and phonons (yellow). The black solid lines are the bare phonon modes, and the black dashed lines are the bare magnon modes. (b),(c) Cartoon representation of the spin fluctuations (projected onto the a - b plane) in the two components of the degenerate magnon mode. (d)–(g) Displacement patterns of all E_{2g} modes. The lengthening (shortening) of the out-of-plane bonds (in magenta) is depicted as thinner (thicker) bonds. The schematics of the molecular-field-induced spin rotation are shown next to each phonon. The black arrow shows the presence and direction of the instantaneous net magnetic moment induced by the perturbation.

and the phonons would cross, which is in striking contrast to the high- T data [Fig. 1(e)]. The avoided crossing is centered at around $L = 0.175$ r.l.u., and the spectral weight of the former bare E_{2g}^+ and E_{2g}^- branches is apparently lost past the hybridization gap due to its transfer into the magnon part of the excitation to which IXS is not sensitive. Most importantly, the third magnon-phonon branch appears at lower energies due to this hybridization that eventually carries most of the spectral weight of the former E_{2g}^+ phonon toward the zone boundary.

Figure 2(b) summarizes the results of the Lorentzian fits of the spectra selectively shown for momenta just below and above the avoided crossing (at $L = 0.15$ and 0.2 r.l.u., respectively). For the former, the fits describe an additional peak of a lesser intensity that appears at ~ 10 meV. In the latter case, the spectral weight redistributes such that the lower and the middle modes have approximately equal intensities, whereas the upper-energy mode is twice weaker. Fitting the peaks, we obtain a large hybridization gap ~ 2 meV. Fits for all momenta can be found in Supplemental Material [44].

Model of the magnon-phonon coupling—To discuss the spin-lattice coupling mechanism, we propose an effective minimal model of the exchange interactions in Mn_3Ge . It consists of two frustrated exchanges and the easy-plane anisotropy that confines the spins in the a - b plane; see Figs. 1(a) and 1(b). We chose our model parameters as $J_1 = 5$, $J_2 = 10$, and $B = 0.1$ meV (see Supplemental Material [44] for further details). Note that the effects of the Dzyaloshinskii-Moriya interaction (DMI) on the ground state and magnons were considered in the recent studies [38,41,45]. It can be shown [44] that from the

magnon's point of view, the DMI can be effectively incorporated into the anisotropy parameter B . This further highlights the universality of the proposed minimal model.

In the low-energy sector near the Γ point, we have three branches of magnons represented by the gapless Nambu-Goldstone mode and doubly degenerate gapped mode. Note that the former is flat [46] for in-plane momenta \mathbf{Q} (i.e., for $L = 0$) and one should add, e.g., next-nearest in-plane exchange, to make it dispersive. However, our goal is to discuss the $\Gamma - A$ path in BZ, and we are not addressing this issue here. Doubly degenerate gapped magnons can be conveniently represented as depicted in Figs. 3(b) and 3(c). We denote the excitations with the net magnetic moment fluctuating along [100] and [120] as the X and Y magnons, respectively. The Y magnon is characterized by one idle spin, one rotating clockwise, and the other rotating counterclockwise. In the X mode, two spins rotate counterclockwise with the same amplitude, and the other rotates clockwise with doubled amplitude.

Using symmetry arguments, it can be easily demonstrated that none of the phonon modes of a single kagome layer (in which the sites are linked by only J_1 or even upon inclusion of farther-neighbor couplings) can lead to significant perturbation of the effective molecular field at any spin site when the phonon momenta are lying in the vicinity of the zone center (see Supplement Material for details [44]). Therefore, all optical modes of the coupled kagome lattice should be considered only with respect to the out-of-plane exchange J_2 , which binds six Mn atoms of the unit cell into separate molecular motifs [Fig. 1(b)]—buckled hexagonal rings.

The in-plane distortions of the hexagonal-ring motifs for the E_{2g} modes can be considered in detail. Each of the lattice vibrations is illustrated in Figs. 3(d)–3(g) along with the schematics of the effective molecular fields acting on each spin sublattice. As the result of such effective molecular fields, which are related to uncompensated strengthening and weakening of the neighboring J_2 bonds, the spin may experience either clockwise or counterclockwise torque. Depending on the combination of the clockwise and counterclockwise rotations of the spins within the hexagonal-ring motif, a net magnetic moment may or may not appear. For convenience, the basis for the doubly degenerate E_{2g} modes was chosen such that two of the six Mn atoms displace strictly either along the [100] (the component x) or [120] (the component y) crystallographic directions.

Only those optical phonons that create the net fluctuating magnetic moment can resonate with the X and Y magnons (see Supplemental Material [44] for analysis of the other phonons), whereas the other modes are blind to the magnetic excitations in the leading order of the spin-lattice Hamiltonian. All four E_{2g} modes that retain two mirror planes and C_2 symmetries produce a net magnetic moment as depicted in Figs. 3(d)–3(g). In the y component of both E_{2g}^- and E_{2g}^+ , one spin of the kagome layer is idle, whereas the other two spins rotate with the same amplitude and with the opposite sense due to an effective molecular field of J_2 . Such a spin rotation pattern exactly matches the eigenvectors of the Y magnon discussed earlier. Moreover, a one-to-one correspondence is found between the X magnon and the x component of the E_{2g} modes. This makes it apparent that two and only two doubly degenerate optical in-plane modes of the E_{2g} symmetry will exhibit a strong coupling with the magnetic fluctuations in the kagome materials.

To be precise, we use J_2 exponential dependence on the bond length in the approximate form

$$J'_2(r) = J_2 \exp\left(-\frac{r}{r_0}\right) \approx J_2 - J_2 \frac{r}{r_0}, \quad (1)$$

where r is the (longitudinal) bond deformation quantized with the phonon operators and r_0 is some constant of the order of Mn 3d orbital size. This phonon-induced variation of J_2 leads to an emergent transverse field for spins and, hence, to the linear coupling in phonon and magnon operators. Importantly, the lattice symmetry dictates the exact form of the transverse fields and magnon “wave functions.” The latter allow only for the $X - x$ and $Y - y$ couplings. Considering only two modes at some particular Q_L , we can write

$$\mathcal{H}_{\text{mag-ph}} = \sum_{n=X,Y} \omega A_n^\dagger A_n - \Delta(A_n + A_n^\dagger)(b_n + b_n^\dagger) + \Omega b_n^\dagger b_n. \quad (2)$$

Here, A and A^\dagger are the magnon operators, b and b^\dagger are the phonon operators, and Δ is weakly dependent on the momentum coupling constant,

$$\Delta \sim \frac{l_0 S^{3/2} J_2}{r_0} \sim 1 \text{ meV}. \quad (3)$$

Parameter $l_0 = \sqrt{\hbar^2/2M_{\text{Mn}}\Omega}$ is another important length scale. It is of the order of magnitude of the quantum mechanical coordinate uncertainty of the Mn ion in the lattice.

The Hamiltonian [Eq. (2)] leads to a system of four equations. However, under an assumption $\omega, \Omega \gg \Delta$ (in agreement with the experimental observations) one can neglect the “fast terms” $A_n b_n$ and $A_n^\dagger b_n^\dagger$. Recalling that we have two relevant phonon modes for each of the X and Y magnons, we arrive at the coupling Hamiltonian

$$\mathcal{H} = \begin{pmatrix} \omega(Q_L) & -\Delta & -\Delta \\ -\Delta & \Omega_-(Q_L) & 0 \\ -\Delta & 0 & \Omega_+(Q_L) \end{pmatrix}. \quad (4)$$

The results are illustrated in Fig. 2(c), where we show the simulated IXS spectral weight of the hybridized modes and the magnon-phonon dispersion relations for the coupling parameter $\Delta = 1$ meV. The spectral weight was simulated for the reciprocal path $(221) - (22\frac{1}{2})$ for direct comparison with the experimental spectra [Fig. 2(a)]. Evidently, a faithful agreement with the experimental data is reached. Figure 3(a) illustrates properties of the Hamiltonian [Eq. (4)] eigenmodes. Note that, even at $L = 0$ (Γ point), phononlike excitations at ≈ 13 and ≈ 17 meV carry $\sim 10\%$ of the magnon amplitude, thus being magnon polarons.

Conclusion—To summarize, our investigation of the kagome material Mn_3Ge has unveiled significant insights into the interplay between spin and lattice dynamics through the observation of dispersive magnetoelastic waves propagating perpendicular to the kagome planes, which is a clear manifestation of strong magnon-phonon coupling. By employing inelastic x-ray scattering combined with *ab initio* calculations and theoretical modeling, we demonstrated that the low-energy excitations in Mn_3Ge are predominantly governed by the interactions between in-plane spin fluctuations and transverse optical phonons. The coupling is facilitated by the noncollinear magnetic order and the comparable energy scales of the magnons and phonons and is enhanced by the prevalence of the magnetic ions in the lattice dynamics.

The effective analytical model provides an excellent fit to the experimental data, further reinforcing the notion that Mn_3Ge serves as an ideal platform for exploring the rich physics of magnon-phonon hybridization. Given the complexity and variety of lattice vibrations in typical triangular antiferromagnets, the clarity offered by a relatively simple

unit cell of Mn₃Ge allows for a more straightforward interpretation of the hybrid modes, bridging theoretical models and experimental observations.

The developed model should be applicable not only to closely related materials such as Mn₃Sn [51,52] and Mn₃Ga [53–55] but also to a broad and abundant class of the kagome antiferromagnets.

Acknowledgments—We thank A. Bosak for his help in sample preparation for the ID28 experiments, planning and conducting the experiments, and interpreting the experimental results. O. I. U. acknowledges financial support from the Institute for Basic Science (IBS), the Republic of Korea (Project No. IBS-R024-D1). A. K. acknowledges the Education Department of the Basque Government (Grant No. PIBA_2023_1_0051). K. M. acknowledges the support of the Department of Atomic Energy, Government of India (Grant No. 58/20/03/2021-BRNS/37084); the Department of Science and Technology, Government of India, through a core research grant (Grant No. CRG/2022/001826); and the Max Planck Society for funding support under the Max Planck-India partner group project. This research was supported through the Emmy Noether program of the German Science Foundation (Project No. 501391385).

Data availability—The data that support the findings of this Letter are not publicly available because they are owned by a third party and the terms of use prevent public distribution. The data are available from the authors upon reasonable request.

- [1] T. W. J. Metzger, K. A. Grishunin, C. Reinhoffer, R. M. Dubrovin, A. Arshad, I. Ilyakov, T. V. A. G. de Oliveira, A. Ponomaryov, J.-C. Deinert, S. Kovalev, R. V. Pisarev, M. I. Katsnelson, B. A. Ivanov, P. H. M. van Loosdrecht, A. V. Kimel, and E. A. Mashkovich, *Nat. Commun.* **15**, 5472 (2024).
- [2] E. A. Mashkovich, K. A. Grishunin, R. M. Dubrovin, A. K. Zvezdin, R. V. Pisarev, and A. V. Kimel, *Science* **374**, 1608 (2021).
- [3] Y. Li, Y. Duan, M. Wang, L. Lang, Y. Zhang, M. Yang, J. Li, W. Fan, K. Shen, Z. Shi, and S.-M. Zhou, *Phys. Rev. Lett.* **132**, 056702 (2024).
- [4] R. Ramos, T. Hioki, Y. Hashimoto, T. Kikkawa, P. Frey, A. J. E. Kreil, V. I. Vasyuchka, A. A. Serga, B. Hillebrands, and E. Saitoh, *Nat. Commun.* **10**, 5162 (2019).
- [5] T. Kikkawa, K. Shen, B. Flebus, R. A. Duine, K. I. Uchida, Z. Qiu, G. E. W. Bauer, and E. Saitoh, *Phys. Rev. Lett.* **117**, 207203 (2016).
- [6] S. Bao, Z.-L. Gu, Y. Shangguan, Z. Huang, J. Liao, X. Zhao, B. Zhang, Z.-Y. Dong, W. Wang, R. Kajimoto, M. Nakamura, T. Fennell, S.-L. Yu, J.-X. Li, and J. Wen, *Nat. Commun.* **14**, 6093 (2023).
- [7] S. Zhang, G. Go, K.-J. Lee, and S. K. Kim, *Phys. Rev. Lett.* **124**, 147204 (2020).
- [8] G. Go, S. K. Kim, and K.-J. Lee, *Phys. Rev. Lett.* **123**, 237207 (2019).
- [9] R. Takahashi and N. Nagaosa, *Phys. Rev. Lett.* **117**, 217205 (2016).
- [10] J. Cui, E. V. Boström, M. Ozerov, F. Wu, Q. Jiang, J.-H. Chu, C. Li, F. Liu, X. Xu, A. Rubio, and Q. Zhang, *Nat. Commun.* **14**, 3396 (2023).
- [11] T. Nomura, X.-X. Zhang, S. Zherlitsyn, J. Wosnitza, Y. Tokura, N. Nagaosa, and S. Seki, *Phys. Rev. Lett.* **122**, 145901 (2019).
- [12] E. Thingstad, A. Kamra, A. Brataas, and A. Sudbø, *Phys. Rev. Lett.* **122**, 107201 (2019).
- [13] H. Hayashi and K. Ando, *Phys. Rev. Lett.* **121**, 237202 (2018).
- [14] C. Chen, P. Liu, S. Liang, Y. Zhang, W. Zhu, L. Han, Q. Wang, S. Fu, F. Pan, and C. Song, *Phys. Rev. Lett.* **133**, 056702 (2024).
- [15] Z. Zhang, F. Y. Gao, Y.-C. Chien, Z.-J. Liu, J. B. Curtis, E. R. Sung, X. Ma, W. Ren, S. Cao, P. Narang, A. von Hoegen, E. Baldini, and K. A. Nelson, *Nat. Phys.* **20**, 788 (2024).
- [16] D. A. Bozhko, P. Clausen, G. A. Melkov, V. S. L'vov, A. Pomyalov, V. I. Vasyuchka, A. V. Chumak, B. Hillebrands, and A. A. Serga, *Phys. Rev. Lett.* **118**, 237201 (2017).
- [17] H. Zhang, C. Xu, C. Carnahan, M. Srtenovic, N. Suri, D. Xiao, and X. Ke, *Phys. Rev. Lett.* **127**, 247202 (2021).
- [18] D. D. Yaremkevich, A. V. Scherbakov, L. De Clerk, S. M. Kukhtaruk, A. Nadzeyka, R. Campion, A. W. Rushforth, S. Savel'ev, A. G. Balanov, and M. Bayer, *Nat. Commun.* **14**, 8296 (2023).
- [19] Q. Wang, A. V. Chumak, and P. Pirro, *Nat. Commun.* **12**, 2636 (2021).
- [20] J. Oh, M. D. Le, H.-H. Nahm, H. Sim, J. Jeong, T. G. Perring, H. Woo, K. Nakajima, S. Ohira-Kawamura, Z. Yamani, Y. Yoshida, H. Eisaki, S. W. Cheong, A. L. Chernyshev, and J.-G. Park, *Nat. Commun.* **7**, 13146 (2016).
- [21] T. Kim, K. Park, J. C. Leiner, and J.-G. Park, *J. Phys. Soc. Jpn.* **88**, 081003 (2019).
- [22] H. Miao, T. T. Zhang, H. X. Li, G. Fabbris, A. H. Said, R. Tartaglia, T. Yilmaz, E. Vescovo, J. X. Yin, S. Murakami, X. L. Feng, K. Jiang, X. L. Wu, A. F. Wang, S. Okamoto, Y. L. Wang, and H. N. Lee, *Nat. Commun.* **14**, 6183 (2023).
- [23] S. Pailhès, X. Fabrèges, L. P. Régnault, L. Pinsard-Godart, I. Mirebeau, F. Moussa, M. Hennion, and S. Petit, *Phys. Rev. B* **79**, 134409 (2009).
- [24] S. L. Holm, A. Kreisel, T. K. Schäffer, A. Bakke, M. Bertelsen, U. B. Hansen, M. Retuerto, J. Larsen, D. Prabhakaran, P. P. Deen, Z. Yamani, J. O. Birk, U. Stuhr, C. Niedermayer, A. L. Fennell, B. M. Andersen, and K. Lefmann, *Phys. Rev. B* **97**, 134304 (2018).
- [25] T. Kim, J. C. Leiner, K. Park, J. Oh, H. Sim, K. Iida, K. Kamazawa, and J.-G. Park, *Phys. Rev. B* **97**, 201113(R) (2018).
- [26] K. Park, J. Oh, K. H. Lee, J. C. Leiner, H. Sim, H.-H. Nahm, T. Kim, J. Jeong, D. Ishikawa, A. Q. R. Baron, and J.-G. Park, *Phys. Rev. B* **102**, 085110 (2020).
- [27] D. Senff, P. Link, K. Hradil, A. Hiess, L. P. Regnault, Y. Sidis, N. Aliouane, D. N. Argyriou, and M. Braden, *Phys. Rev. Lett.* **98**, 137206 (2007).
- [28] S. Petit, F. Moussa, M. Hennion, S. Pailhès, L. Pinsard-Gaudart, and A. Ivanov, *Phys. Rev. Lett.* **99**, 266604 (2007).

- [29] X. Fabrèges, S. Petit, I. Mirebeau, S. Pailhès, L. Pinsard, A. Forget, M. T. Fernandez-Diaz, and F. Porcher, *Phys. Rev. Lett.* **103**, 067204 (2009).
- [30] S. Tóth, B. Wehinger, K. Rolfs, T. Birol, U. Stuhr, H. Takatsu, K. Kimura, T. Kimura, H. M. Rønnow, and C. Rüegg, *Nat. Commun.* **7**, 13547 (2016).
- [31] J. H. Kim and J. H. Han, *Phys. Rev. B* **76**, 054431 (2007).
- [32] X.-Y. Chen and Y.-P. Wang, *Phys. Rev. B* **104**, 155132 (2021).
- [33] H. Yang, Y. Sun, Y. Zhang, W.-J. Shi, S. S. P. Parkin, and B. Yan, *New J. Phys.* **19**, 015008 (2017).
- [34] J. Liu and L. Balents, *Phys. Rev. Lett.* **119**, 087202 (2017).
- [35] A. K. Nayak, J. E. Fischer, Y. Sun, B. Yan, J. Karel, A. C. Komarek, C. Shekhar, N. Kumar, W. Schnelle, J. Kübler, C. Felser, and S. S. P. Parkin, *Sci. Adv.* **2**, e1501870 (2016).
- [36] J. Kübler and C. Felser, *Europhys. Lett.* **108**, 67001 (2014).
- [37] T. Nagamiya, S. Tomiyoshi, and Y. Yamaguchi, *Solid State Commun.* **42**, 385 (1982).
- [38] J.-R. Soh, F. de Juan, N. Qureshi, H. Jacobsen, H.-Y. Wang, Y.-F. Guo, and A. T. Boothroyd, *Phys. Rev. B* **101**, 140411(R) (2020).
- [39] A. S. Sukhanov, S. Singh, L. Caron, T. Hansen, A. Hoser, V. Kumar, H. Borrmann, A. Fitch, P. Devi, K. Manna, C. Felser, and D. S. Inosov, *Phys. Rev. B* **97**, 214402 (2018).
- [40] J. W. Cable, N. Wakabayashi, and P. Radhakrishna, *Phys. Rev. B* **48**, 6159 (1993).
- [41] Y. Chen, J. Gaudet, S. Dasgupta, G. G. Marcus, J. Lin, T. Chen, T. Tomita, M. Ikhlas, Y. Zhao, W. C. Chen, M. B. Stone, O. Tchernyshyov, S. Nakatsuji, and C. Broholm, *Phys. Rev. B* **102**, 054403 (2020).
- [42] A. Zelenskiy, T. L. Monchesky, M. L. Plumer, and B. W. Southern, *Phys. Rev. B* **103**, 144401 (2021).
- [43] A. S. Sukhanov, M. S. Pavlovskii, P. Bourges, H. C. Walker, K. Manna, C. Felser, and D. S. Inosov, *Phys. Rev. B* **99**, 214445 (2019).
- [44] See Supplemental Material at <http://link.aps.org/supplemental/10.1103/gymx-jk1g> for the extended theory of the magnon-phonon coupling in Mn₃Ge and additional details on the simulated IXS intensity and additional analysis of the experimental data [30,38,40,41,43,45,46–50].
- [45] S. Dasgupta and O. Tchernyshyov, *Phys. Rev. B* **102**, 144417 (2020).
- [46] D. Leykam, A. Andreev, and S. Flach, *Adv. Phys.* **3**, 1473052 (2018).
- [47] T. Holstein and H. Primakoff, *Phys. Rev.* **58**, 1098 (1940).
- [48] R. Gekht, *Zh. Eksp. Teor. Fiz.* **87**, 2095 (1984) [Sov. Phys. JETP **60**, 1210 (1984)].
- [49] A. L. Chernyshev, *Phys. Rev. B* **92**, 094409 (2015).
- [50] N. Kiyohara, T. Tomita, and S. Nakatsuji, *Phys. Rev. Appl.* **5**, 064009 (2016).
- [51] P. Park, J. Oh, K. Uhlířová, J. Jackson, A. Deák, L. Szunyogh, K. H. Lee, H. Cho, H.-L. Kim, H. C. Walker, D. Adroja, V. Sechovský, and J.-G. Park, *npj Quantum Mater.* **3**, 63 (2018).
- [52] Q. Meng, J. Dong, P. Nie, L. Xu, J. Wang, S. Jiang, H. Zuo, J. Zhang, X. Li, Z. Zhu, L. Balents, and K. Behnia, *Nat. Commun.* **15**, 6921 (2024).
- [53] J. Železný, Y. Zhang, C. Felser, and B. Yan, *Phys. Rev. Lett.* **119**, 187204 (2017).
- [54] B. B. Singh, K. Roy, J. A. Chelvane, and S. Bedanta, *Phys. Rev. B* **102**, 174444 (2020).
- [55] M. Raju, R. Romero, D. Nishio-Hamane, R. Uesugi, M. Asakura, Z. Tagay, T. Higo, N. P. Armitage, C. Broholm, and S. Nakatsuji, *Phys. Rev. Mater.* **8**, 014204 (2024).
- [56] M. Krisch and F. Sette, *Crystallogr. Rep. (Transl. Kristallografiya)* **62**, 1 (2017).
- [57] G. Kresse and D. Joubert, *Phys. Rev. B* **59**, 1758 (1999).
- [58] G. Kresse and J. Furthmüller, *Phys. Rev. B* **54**, 11169 (1996).
- [59] G. Kresse and J. Furthmüller, *Comput. Mater. Sci.* **6**, 15 (1996).
- [60] J. P. Perdew, K. Burke, and M. Ernzerhof, *Phys. Rev. Lett.* **77**, 3865 (1996).
- [61] A. Togo and I. Tanaka, *Scr. Mater.* **108**, 1 (2015).

End Matter

Sample preparation—A high-quality single crystal of Mn₃Ge was grown using the Bridgman–Stockbarger technique as described in Ref. [35]. The crystal was milled and polished mechanically down to a ~100 μm thick rod to ensure low x-ray attenuation in transmission geometry. All measurements were conducted on the same sample unless explicitly specified. Additional measurements were conducted on another piece of crystal cut from the same bulk specimen (see Supplemental Material [44]).

Inelastic x-ray scattering experiments—High-resolution IXS measurements were performed at the beamline ID28 [56] at ESRF (Grenoble, France). The incident energy was varied by controlling the temperature of a Si (999) monochromator, whereas the outgoing energy was fixed at 17.8 keV by a Si (999) analyzer. The resulting energy

resolution defined as the full width at half maximum of a Lorentzian peak profile in this setup amounts to ~3 meV, which was independently verified by measurements of the elastic line in our setup. To map out the dispersion of the pure phonon and hybridized magnon-phonon modes, we collected IXS spectra at many points along the high-symmetry momenta in reciprocal space with a fine step. We used a cryostream cooling system for measurements down to 80 K. The same setup was used to measure the sample on heating up to 500 K. To fit the IXS spectra for each momenta, we fixed the peak width to the instrumental resolution, which allows for reducing the number of free parameters. The independent fit parameters are thus the peak positions and peak intensities (area below the peak).

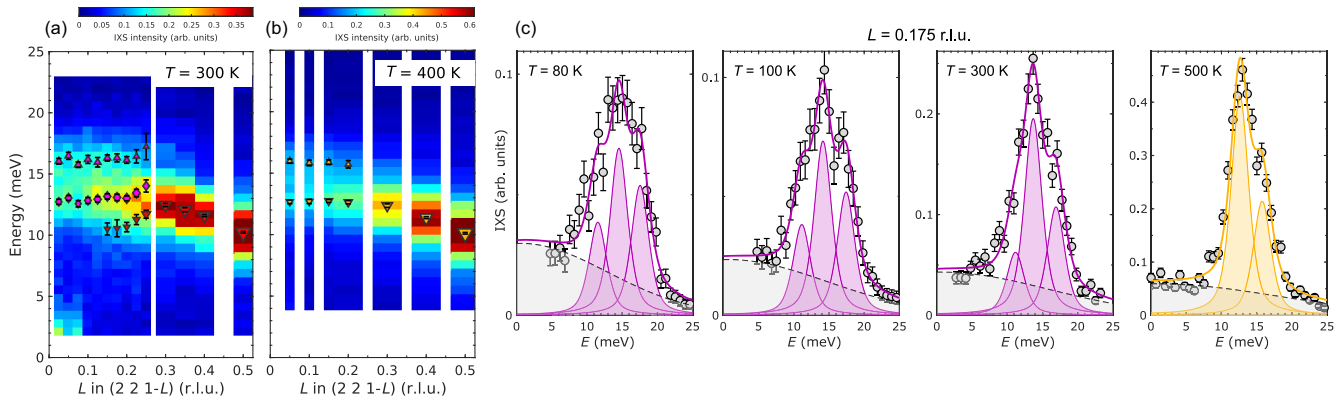


FIG. 4. Energy-momenta maps of the IXS intensity at 300 K (a) and 400 K (b). The symbols are the results of the peak fits (see the main text). (c) IXS spectra collected at momenta of (2 2 0.825) r.l.u. at different temperatures. The symbols are the data, the shaded areas are the individual peak contributions in the total fit function (solid line), and the dashed line is the background contribution. The error bars represent 1σ uncertainty.

First-principle simulations of the bare phonon modes—To simulate the lattice dynamics of Mn_3Ge in the limit of decoupled magnons and phonons, we performed *ab initio* calculations using the projector-augmented wave method [57] within density functional theory, as implemented in the VASP package [58,59]. We used the generalized gradient approximation functionals with Perdew-Burke-Ernzerhof parametrization [60]. Magnetic moments of Mn ions, which form the noncollinear magnetic structure, were taken into account by performing spin-polarized calculations. The phonons were calculated by constructing a $(2 \times 2 \times 2)$ supercell and calculating the force constants using the small-displacement method implemented in PHONOPY [61]. An additional phase can be introduced to the output eigenvectors to allow for better agreement with the experimental IXS intensities (see Supplemental Material [44]).

Simulation of the inelastic x-ray scattering—The IXS phonon spectral weight was simulated using direct numerical evaluations of the scattering cross section for the one-phonon scattering:

$$S(\mathbf{Q}, E) \propto \sum_{s, \mathbf{q}, \tau} \frac{1}{E_s(\mathbf{q})} \left| \sum_d \frac{\rho(\mathbf{Q})_d}{\sqrt{M_d}} e^{i\mathbf{Q} \cdot \mathbf{r}_d} e^{-W_d} (\mathbf{Q} \cdot \epsilon_{d,s}) \right|^2 \times \langle n_s + 1 \rangle \delta[E_s(\mathbf{q}) - E] \delta(\mathbf{Q} - \mathbf{q} - \tau), \quad (\text{D1})$$

where E and $\epsilon_{d,s}$ are the energy and polarization, respectively, of the phonon with the mode index s and the wave vector \mathbf{q} ; τ is a reciprocal lattice vector; \mathbf{r}_d is the position vector for the atom d in the unit cell; M_d is its mass and $\rho(\mathbf{Q})_d$ is its Fourier transform of the electron density; W_d is the Debye–Waller factor; and n_s is the Bose–Einstein distribution.

The simulated intensity was convoluted with the resolution function of the ID28 spectrometer. Prior to

experimental measurements, we used simulated intensity for extensive screening of the momentum space to locate the Brillouin zone (BZ) indices where the phonon modes of interest (i) carry significant spectral weight and (ii) are not spectrally contaminated by the other, not relevant, branches.

Additional IXS data collected at intermediate temperatures—For the discussion of the main results, we focus on the comparative IXS data analysis for the spectra collected at the lowest accessible (using a cryostream sample environment) temperature of 80 K and at a high temperature of 500 K, which is well above the $T_N \approx 370$ K. Naive expectations are that at intermediate temperatures $80 \text{ K} < T < T_N$ the avoided mode crossing will be less pronounced. Here, we show additional data collected at 300 K [Fig. 4(a)], which is just below the ordering temperature, and at 400 K [Fig. 4(b)], i.e., just above it.

Whereas the spectra at 80 K feature an abrupt modulation in intensity around the avoided-crossing momenta $\sim 0.175 \text{ r.l.u.}$, the spectra at 300 K are characterized by a more homogeneous intensity distribution over momenta. Each individual IXS spectrum of the map was fitted by the same model of three peaks. The results were plotted over the intensity map in Fig. 4(a). As can be seen, all modes in the vicinity of the avoided crossing reduced their slope at 300 K, as expected from the softened magnons at temperatures relatively close to T_N .

Along with expectations, the hybridization gaps close as soon as the sample is heated above T_N , as evidenced by the intensity map for 400 K [Fig. 4(b)]. The spectra at 400 and 500 K (the main text) turn out to show very similar intensity distributions and can be characterized by only two bare phonon modes.

The temperature variations in the magnon-phonon spectra are highlighted in Fig. 4(c), where we plot the spectra collected at the same momenta of (2 2 0.825) r.l.u. for

$T = 80, 100, 300$, and 500 K. The spectrum at such a momentum has been omitted in the measurements at 400 K, thus a direct comparison is not possible. However, the 400 K spectra at $L = 0.15$ and 0.2 r.l.u. suggest the exact same trend. As can be seen, the intensity of the lower mode (~ 10 meV) is significantly reduced at 300 K and redistributed into the middle (~ 14 meV) branch. The same, but

to a lesser extent, applies to the upper (~ 17 meV) branch. Since the observed IXS intensity is directly proportional to the phonon weight in the magnon-phonon wave function, it is obvious that the mode hybridization weakens at temperatures close to the magnetic ordering, whereas the avoided-crossing momentum shifts outward due to softening of the bare magnons.